

Analytical and numerical models of viscous anisotropy: a toolset to constrain the role of mechanical anisotropy for regional tectonics and fault loading

Dunyu Liu¹, Simone Puel^{1,2,†}, Thorsten W. Becker^{1,2,3} and Louis Moresi⁴

¹*Institute for Geophysics, Jackson School of Geosciences, The University of Texas at Austin, 78758, Austin, USA. nding. E-mail: dliu@ig.utexas.edu*

²*Department of Earth and Planetary Sciences, Jackson School of Geosciences, The University of Texas at Austin, 78712, Austin, USA*

³*Oden Institute for Computational Engineering and Sciences, The University of Texas at Austin, 78712, Austin, USA*

⁴*Research School of Earth Science, Australian National University, ACT 2601, Canberra, Australia*

Accepted 2024 August 20. Received 2024 August 19; in original form 2024 June 24

SUMMARY

To what extent mechanical anisotropy is required to explain the dynamics of the lithosphere is an important yet unresolved question. If anisotropy affects stress and deformation, and hence processes such as fault loading, how can we quantify its role from observations? Here, we derive analytical solutions and build a theoretical framework to explore how a shear zone with linear anisotropic viscosity can lead to deviatoric stress heterogeneity, strain-rate enhancement, as well as non-coaxial principal stress and strain rate. We develop an open-source finite-element software based on *FEniCS* for more complicated scenarios in both 2-D and 3-D. Mechanics of shear zones with transversely isotropic and orthorhombic anisotropy subjected to misoriented shortening and simple shearing are explored. A simple regional example for potential non-coaxiality for the Leech River Schist above the Cascadia subduction zone is presented. Our findings and these tools may help to better understand, detect and evaluate mechanical anisotropy in natural settings, with potential implications including the transfer of lithospheric stress and deformation through fault loading.

Key words: Finite element method; Numerical modelling; Dynamics and mechanics of faulting; Mechanics, theory, and modelling; Rheology: crust and lithosphere.

1 INTRODUCTION

Mechanical anisotropy can refer to either elastic moduli (e.g. Babuska & Cara 1991), plastic dilatancy (e.g. Rawling *et al.* 2002) or creep viscosities (e.g. Vauchez *et al.* 1998) depending on the deformation mechanisms. Elastoplastic anisotropy is important for seismic wave propagation or damage/fracture development. The viscous, long-term deformation type of mechanical anisotropy matters for flow, where examples include ice sheets and mantle convection including lithospheric deformation, on which we focus here.

Viscous anisotropy of the crust and lithospheric mantle may be caused by the effects of melt (e.g. Takei & Katz 2013), embedded structural zones of weakness (shape preferred orientation, SPO; e.g. Montési 2013), superposition of different scales of asthenospheric, power law flow (Schmeling 1985), or may be due to crystallographically preferred orientation (CPO), for example, of intrinsically

anisotropic olivine crystals (Tommasi *et al.* 2009; Hansen *et al.* 2016).

The resulting mechanical anisotropy can be preserved at distributed lithospheric scale within presently inactive, formerly deformed sutures, that is, tectonic inheritance, or concentrated into narrow shear zones within active plate boundaries (e.g. Vauchez *et al.* 1998; Mühlhaus *et al.* 2004). Spatial variations in mechanical anisotropy may result in strain localization in plate interiors that may affect flexural strength (e.g. Simons & van der Hilst 2003) or play a role for intraplate seismicity (Mameri *et al.* 2021).

Olivine-aggregate deformation experiments show textures with significant viscous anisotropy (e.g. Hansen *et al.* 2016). Mechanical anisotropy is thus expected as a result of CPOs, and the development of the latter is explored widely in the context of connecting mantle flow and seismic anisotropy (e.g. Becker *et al.* 2006; Becker & Lebedev 2021). Any feedback between mechanical anisotropy and convection may then affect the predictions for seismic anisotropy, for example (e.g. Chastel *et al.* 1993; Blackman *et al.* 2017).

[†]Now at: Seismological Laboratory, Division of Geological and Planetary Sciences, California Institute of Technology.

However, at least within an instantaneous mantle flow or lithospheric deformation scenario, mechanical anisotropy can be hard to distinguish from isotropic weakening (Becker & Kawakatsu 2011; Ghosh *et al.* 2013). Time-dependent scenarios of deformation are expected to be more affected by mechanical anisotropy compared to isotropic zones of weakness, for example, for lithospheric instabilities and shear zones (Mühlhaus *et al.* 2004; Lev & Hager 2008, 2011; Perry-Houts & Karlstrom 2019), for post-glacial rebound (Schmeling 1985; Han & Wahr 1997), or on plate scales (Honda 1986; Christensen 1987; Király *et al.* 2020).

It is thus important to further constrain the role of mechanical anisotropy for the lithosphere, and observations from tectonically well-constrained regional settings provide an opportunity to explore complementary strain and stress sensitive data (e.g. Mameri *et al.* 2021; Schulte-Pelkum *et al.* 2021). In turn, mechanical anisotropy may affect some of the methods used to infer stress or stressing rate close to faults, such as inversion of focal mechanisms (e.g. Kaven *et al.* 2011). In Southern California, for example, inherited CPOs and alignment of weak layers through SPO could both be a source of mechanical anisotropy. This could possibly explain some of the mismatch between geodetically inferred strain rates and focal-mechanism-derived stress close to faults, and the re-activation of pre-existing fault structures may affect the tectonic deformation response and local fault loading (Schulte-Pelkum *et al.* 2021, and references therein).

Studies that explore the effects of mechanical anisotropy on regional scales for Southern California are, however, still limited. Ghosh *et al.* (2013) implemented an anisotropic San Andreas Fault (SAF) as a shear zone in a 3-D global, viscous deformation model but failed to identify robust indicators of mechanical anisotropy on regional scales. However, if mechanical anisotropy is considered in a regional scale model, it may be easier to assess the documented non-coaxiality between stress and strain (Schulte-Pelkum *et al.* 2021), and to eventually incorporate time dependence in a field-observation validated way. This suggests an opportunity to develop new methods for inferring mechanical anisotropy from field observations and further constrain fault loading.

In this study, we work toward a theoretical framework and first solve analytically the deformation of a simple 2-D model with a viscously anisotropic layer which highlights some of its fundamental mechanical behaviour. The solution shows stress heterogeneity, strain-rate enhancement, and non-coaxial principal stress and strain rates inside the anisotropic layer and reveals the mechanics behind such heterogeneity. We explore how the orientation and strength of mechanical anisotropy affect the non-coaxiality, stress heterogeneity and strain-rate enhancement. Second, we present a new, open-source finite-element tool, its validation against the analytical solution, and applications to more complex 3-D scenarios. Lastly, we discuss the implications and potential applications of the method and tools.

2 THE 1-D ANALYTICAL SOLUTION OF A VISCOUSLY ANISOTROPIC LAYER SUBJECTED TO SIMPLE SHEARING

Motivated by the not necessarily intuitive solutions produced by earlier numerical tests for mechanical anisotropy, for example, based on our implementations (Moresi *et al.* 2003; Becker & Kawakatsu 2011), we proceed to solve analytically the incompressible Stokes flow equation for a layered model subjected to simple shearing over the thickness, where a central viscously anisotropic layer is sandwiched between two isotropic layers (Fig. 1).

2.1 Governing equations and rheology

The general boundary-value problem of incompressible Stokes flow equation is described by the force balance for a continuum (eq. 1) and the incompressible fluid assumption (eq. 2) at any point in a domain Ω ,

$$\nabla \cdot \sigma + \mathbf{f} = 0, \quad (1)$$

$$\nabla \cdot \mathbf{v} = 0, \quad (2)$$

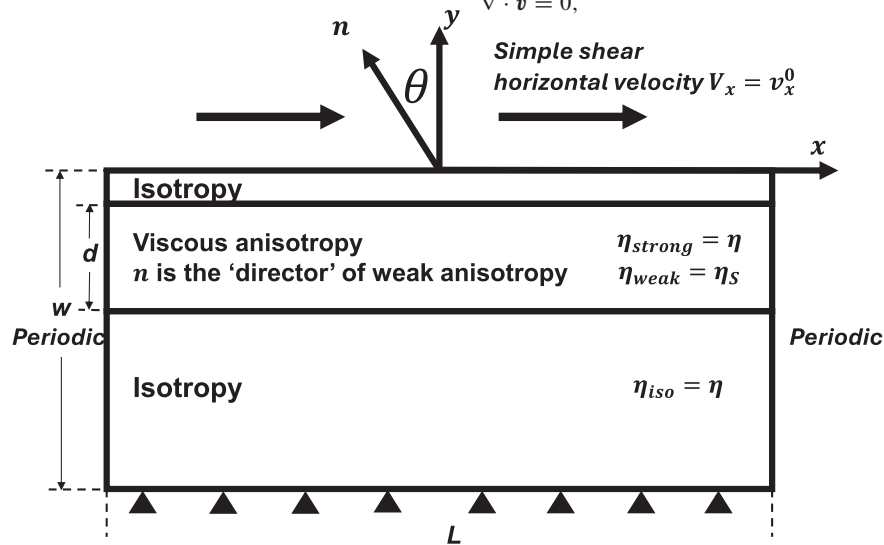


Figure 1. Schematic diagram of the 2-D layered model with a viscously anisotropic layer subjected to simple shearing. \mathbf{n} is the ‘director’ of weak viscous (η_{weak}) direction. The viscosity of the strong direction in the anisotropic layer and the isotropic viscosity are η_{strong} and η_{iso} , respectively. The model domain is L by w with the anisotropic layer with a thickness of d . The angle θ is counted counterclockwise from the y axis to \mathbf{n} . The bottom of the model is no slip, zero velocity. The top of the model shears horizontally with a velocity of v_x^0 . Velocity and pressure on the west and east boundaries are periodic, and the 1-D analytical solution applies with thickness.

where σ is the stress tensor, \mathbf{f} is the body force and \mathbf{v} is the velocity field. We use an incompressible, Newtonian flow constitutive law such that

$$\sigma = -p\mathbf{I} + \tau, \quad (3)$$

$$\tau = \mathbf{D}\dot{\epsilon}, \quad (4)$$

$$\dot{\epsilon} = \frac{\nabla \mathbf{v} + \nabla \mathbf{v}^T}{2}, \quad (5)$$

where p is pressure, τ the deviatoric stress tensor, \mathbf{D} the fourth-order viscosity tensor, \mathbf{I} the identity matrix and $\dot{\epsilon}$ the strain-rate tensor.

For isotropic and anisotropic domains, the viscosity \mathbf{D} will be \mathbf{D}_{iso} and \mathbf{D}_{ani} , respectively. In the isotropic domains,

$$\tau = \mathbf{D}_{\text{iso}}\dot{\epsilon} = 2\eta\dot{\epsilon} = \eta(\nabla \mathbf{v} + \nabla \mathbf{v}^T) \quad (6)$$

with scalar dynamic viscosity η . In the anisotropic domains,

$$\tau = \mathbf{D}_{\text{ani}}\dot{\epsilon}. \quad (7)$$

The \mathbf{D}_{ani} tensor needs not have any symmetry properties, but we start by analysing some simple cases. The highest non-isotropic symmetry case is transverse isotropy (TI), also called ‘hexagonal anisotropy’ in the seismic anisotropy context. A seismically radially or azimuthally anisotropic medium corresponds to TI with a symmetry axis in the vertical or horizontal, respectively. We expect most olivine-associated CPOs in the upper mantle to be predominantly of TI/hexagonal character, with secondary effects due to the lower symmetry, orthorhombic contributions (Browaeys & Chevrot 2004; Becker *et al.* 2006).

Here, we solve a system with linear, transversely anisotropic rheology following formulations in Mühlhaus *et al.* (2002) and Moresi & Mühlhaus (2006) (MM TI anisotropy) with \mathbf{n} the ‘director’ of the weak viscous direction. Following eq. (3) in Mühlhaus *et al.* (2002),

$$\tau_{ij} = 2\eta\dot{\epsilon}_{ij} - 2(\eta - \eta_S)\Lambda_{ijkl}\dot{\epsilon}_{kl}, \quad (8a)$$

$$\Lambda_{ijkl} = \left(\frac{1}{2}(n_i n_k \delta_{lj} + n_j n_k \delta_{il} + n_i n_l \delta_{kj} + n_j n_l \delta_{ik}) - 2n_i n_j n_k n_l \right), \quad (8b)$$

where in n_i ($i = x, y$) is the components of the normal ‘director’, η is the ‘normal’ shear viscosity and η_S is the weak shear viscosity along the weak layer. $i, j, k, l = x, y$. As shown in Fig. 1, θ is the angle between \mathbf{n} and axis y , and then $n_x = -\sin(\theta)$, $n_y = \cos(\theta)$ (cf. Christensen 1985).

A general set of boundary conditions on the boundary $\partial\Omega = \Gamma_D \cup \Gamma_N$ is given by

$$\mathbf{v} = \mathbf{v}_0 \text{ on } \Gamma_D, \quad (9a)$$

$$\nabla \mathbf{v} \cdot \mathbf{n}_N + p\mathbf{n}_N = \mathbf{g} \text{ on } \Gamma_N, \quad (9b)$$

where Γ_D and Γ_N stand for Dirichlet and Neumann boundaries, respectively, and \mathbf{n}_N is the normal to Γ_N .

2.2 Solution specifics

For our example problem, we choose as boundary conditions

$$v_x = v_x^0 \text{ on } \Gamma_D|_{y=0}, \quad (10a)$$

$$v_x = 0, \quad v_y = 0 \text{ on } \Gamma_D|_{y=-w}, \quad (10b)$$

$$\text{periodic on } \Gamma_D|_{x=\pm L/2}, \quad (10c)$$

where a horizontal velocity v_x^0 is applied to the top side, no velocity at the bottom, and periodic velocity and pressure on the west and east sides. Given the symmetry of model geometry and boundary conditions along x , the velocity, pressure, and stress are invariant along x , and vertical velocity is zero, which give

$$v_y = 0; \quad v_{x,x} = 0; \quad \sigma_{ij,x} = 0; \quad p_{,x} = 0 \quad (11)$$

where, for example, $v_{x,x}$ stands for $\frac{\partial v_x}{\partial x}$, and $i, j = x, y$. Therefore, we solve the 1-D analytical solution of velocity, pressure and stress along the vertical thickness (y axis).

Substituting eq. (11) into eq. (5), we get

$$\dot{\epsilon}_{xx} = v_{x,x} = 0 \quad (12a)$$

$$\dot{\epsilon}_{yy} = v_{y,y} = 0 \quad (12b)$$

$$\dot{\epsilon}_{xy} = \frac{v_{x,y} + v_{y,x}}{2} = \frac{v_{x,y}}{2}. \quad (12c)$$

In the isotropic layer, the deviatoric stress components follow as

$$\tau_{xx} = \tau_{yy} = 0 \quad (13a)$$

$$\tau_{xy} = \eta v_{x,y} \quad (13b)$$

In the anisotropic layer, following eq. (8), the deviatoric stress components are

$$\tau_{xx} = -2(\eta - \eta_S)(n_x n_y - 2n_x^3 n_y) v_{x,y} \quad (14a)$$

$$\tau_{xy} = \eta v_{x,y} - (\eta - \eta_S)(1 - 4n_x^2 n_y^2) v_{x,y} \quad (14b)$$

$$\tau_{yy} = -2(\eta - \eta_S)(n_x n_y - 2n_x n_y^3) v_{x,y} \quad (14c)$$

The task now is to find solutions of velocity gradients $v_{x,y}$ in the isotropic (s_1) and anisotropic (s_2) layers. Eq. (13) gives

$$\tau_{xx} = \tau_{yy} = 0, \quad \tau_{xy} = \eta s_1 \quad (15)$$

and eq. (14) yields

$$\tau_{xx} = -2(\eta - \eta_S)(n_x n_y - 2n_x^3 n_y) s_2 \quad (16a)$$

$$\tau_{xy} = \eta s_2 - (\eta - \eta_S)(1 - 4n_x^2 n_y^2) s_2 \quad (16b)$$

$$\tau_{yy} = -2(\eta - \eta_S)(n_x n_y - 2n_x n_y^3) s_2 \quad (16c)$$

The continuity condition for shear stress τ_{xy} and normal stress $\tau_{yy} + p$ on the interfaces between the isotropic and anisotropic layers require

$$\eta s_1 = \eta s_2 - (\eta - \eta_S)(1 - 4n_x^2 n_y^2) s_2, \quad (17)$$

$$p^{\text{iso}} = -2(\eta - \eta_S)(n_x n_y - 2n_x n_y^3) s_2 + p^{\text{aniso}} \quad (18)$$

where p^{iso} and p^{aniso} are pressures inside the isotropic and anisotropic layers, respectively.

The boundary condition for $v_x(y=0) = v_x^0$ and $v_x(y=-w) = 0$ and the integration of $v_{x,y}$ over the entire thickness w can be expressed as

$$\int_{-w}^0 v_{x,y} dy = v_x|_0 - v_x|^{-w} = v_x^0, \quad (19)$$

which gives

$$\int_{-w}^0 v_{x,y} dy = \int_{-d}^0 s_2 dy + \int_{-w}^{-d} s_1 dy = s_2 d + (w-d)s_1 = v_x^0. \quad (20)$$

Solving eqs (17) and (20), we get

$$s_1 = v_x^0 \frac{1 - \left(1 - \frac{\eta_S}{\eta}\right) (1 - 4n_x^2 n_y^2)}{w - \left(1 - \frac{\eta_S}{\eta}\right) (1 - 4n_x^2 n_y^2) (w-d)}, \quad (21a)$$

$$s_2 = \frac{v_x^0}{w - \left(1 - \frac{\eta_S}{\eta}\right) (1 - 4n_x^2 n_y^2) (w-d)}. \quad (21b)$$

Substituting s_1 and s_2 to eqs (15), (16) and (18), we get solutions for velocities, stresses and pressure as a function of thickness y . Substituting s_1 and s_2 to eq. (12), we get the expressions for shear strain rate in the isotropic and anisotropic layers as

$$\dot{\epsilon}_{xy}^{\text{iso}} = v_x^0 \frac{\frac{\eta_S}{\eta} (1 - 4n_x^2 n_y^2) + 4n_x^2 n_y^2}{2 \left[w - \left(1 - \frac{\eta_S}{\eta}\right) (1 - 4n_x^2 n_y^2) (w-d) \right]}, \quad (22a)$$

$$\dot{\epsilon}_{xy}^{\text{ani}} = \frac{v_x^0}{2 \left[w - \left(1 - \frac{\eta_S}{\eta}\right) (1 - 4n_x^2 n_y^2) (w-d) \right]}. \quad (22b)$$

We use the square root of the J_2 , deviatoric invariant of strain-rate tensor to measure the deformation, and in 2-D

$$J_2 = \frac{1}{2} I_1^2 - I_2 = \frac{1}{2} (\dot{\epsilon}_{xx}^2 + \dot{\epsilon}_{yy}^2 + 2\dot{\epsilon}_{xy}^2) = \dot{\epsilon}_{xy}^2. \quad (23)$$

Then, in the isotropic and anisotropic layers,

$$\sqrt{J_2^{\text{iso}}} = |\dot{\epsilon}_{xy}^{\text{iso}}|, \quad (24a)$$

$$\sqrt{J_2^{\text{ani}}} = |\dot{\epsilon}_{xy}^{\text{ani}}|. \quad (24b)$$

We define the ratio between square root of J_2 invariant of the strain-rate tensor in anisotropic and isotropic layers ϕ as strain-rate enhancement to measure the heterogeneity of deformation caused by mechanical anisotropy, and

$$\phi = \frac{\frac{\eta}{\eta_S}}{1 - 4n_x^2 n_y^2 + 4\frac{\eta}{\eta_S} n_x^2 n_y^2}. \quad (25)$$

If we further define viscosity contrast $\gamma = \frac{\eta}{\eta_S}$,

$$\phi = \frac{\gamma}{1 - 4n_x^2 n_y^2 + 4\gamma n_x^2 n_y^2}. \quad (26)$$

The solutions of velocities, strain rates and amplitudes of stresses and pressure for cases with θ are identical to those with $180^\circ - \theta$ as

shown in eqs (16), (18), (21) and (22), respectively, given the symmetric model geometry, transversely isotropic viscosity and loading condition relative to the vertical axis. Results become more complex for 3-D and/or orthorhombic viscosity that is misoriented from the anisotropic layer and loading, as will be shown later.

2.3 The character of the analytical solution

We compute a scenario with $w = 1$, $\eta = 1$, $v_x^0 = 1$ and $d = 0.4$ (thickness between -0.1 and -0.5) with variables defined as in Fig. 1. We change the director \mathbf{n} of the weak viscous direction by varying θ from 0° to 90° , and the viscosity contrast $\gamma = \eta/\eta_S$ in the anisotropic layer to explore their effects on stress and strain-rate. We first set $\gamma = 10$.

Fig. 2 shows the maximum principal stress σ_1 (white bars) and maximum principal strain rate $\dot{\epsilon}_1$ (red bars) between -0.45 and -0.55 thickness, and the maximum shear stress σ_{xy}^{max} (background) between -0.4 and -0.6 thickness, for various θ s. Sharp changes of physical quantities occur at the isotropic-anisotropic interface at -0.5 thickness. In the anisotropic layer, principal stress axes are mismatched at an angle α to the principal strain-rate axes, which are always at 45° to the horizontal axis. The mismatch occurs for a wide range of θ and the magnitude of α depends on θ . The maximum α is $\sim 27.45^\circ$. With increasing θ from 0° , α increases from 0° to the peak of $\sim 27.45^\circ$ when $\theta = 8.8^\circ$, and then decreases to 0° when θ reaches 45° . When θ further increases from 45° , α increases from 0° again to $\sim 27.45^\circ$ but with sign reversed until $\theta = 81.2^\circ$, then decreases to 0° when θ reaches 90° .

Fig. 3(a) shows the angles between σ_1 , $\dot{\epsilon}_1$ and \mathbf{n} as a function of θ in the anisotropic layer for γ of 2, 10 and 100, respectively. θ_1 and θ_2 are angles between σ_1 and \mathbf{n} , and between $\dot{\epsilon}_1$ and \mathbf{n} , respectively. The mismatch $\alpha = \theta_1 - \theta_2$. For all γ s, α increases with increasing θ starting from 0° , reaches to a maximum, and then decreases to 0° when θ reaches 45° . The maximum α depends on viscosity contrast γ . With the larger γ of 100, the maximum $\alpha = \sim 38^\circ$ at $\theta = \sim 3^\circ$. With the smaller γ of 2, the maximum α is $\sim 10^\circ$ at $\theta = \sim 18^\circ$.

The maximum α for a wider range of γ and the corresponding θ that this maximum α is achieved is shown in Fig. 4. If γ is close to 1, α will approach to zero and the model recovers the isotropic scenario. If γ increases, α will increase to the maximum 45° when θ approaches to zero, akin to deformation along the weak anisotropic direction being a stress-free boundary. For $\gamma = 10$, perhaps appropriate for olivine CPOs (Hansen *et al.* 2012), the maximum angular mismatch α could be as large as about 27.45° when $\theta = 8.8^\circ$.

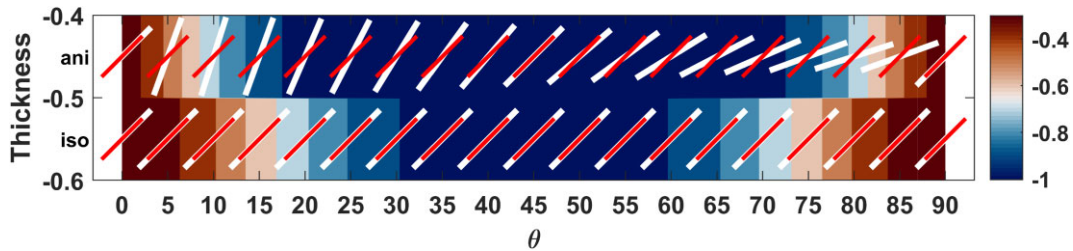


Figure 2. Principal stress σ_1 (longer, white bars), principal strain rate $\dot{\epsilon}_1$ (shorter, red bars) and maximum shear stress σ_{xy}^{max} (background with the colour bar) as a function of θ with viscosity contrast of 10. The isotropic–anisotropic interface is at -0.5 thickness, and the domain above is anisotropic and below is isotropic, as indicated by ‘ani’ and ‘iso’, respectively.

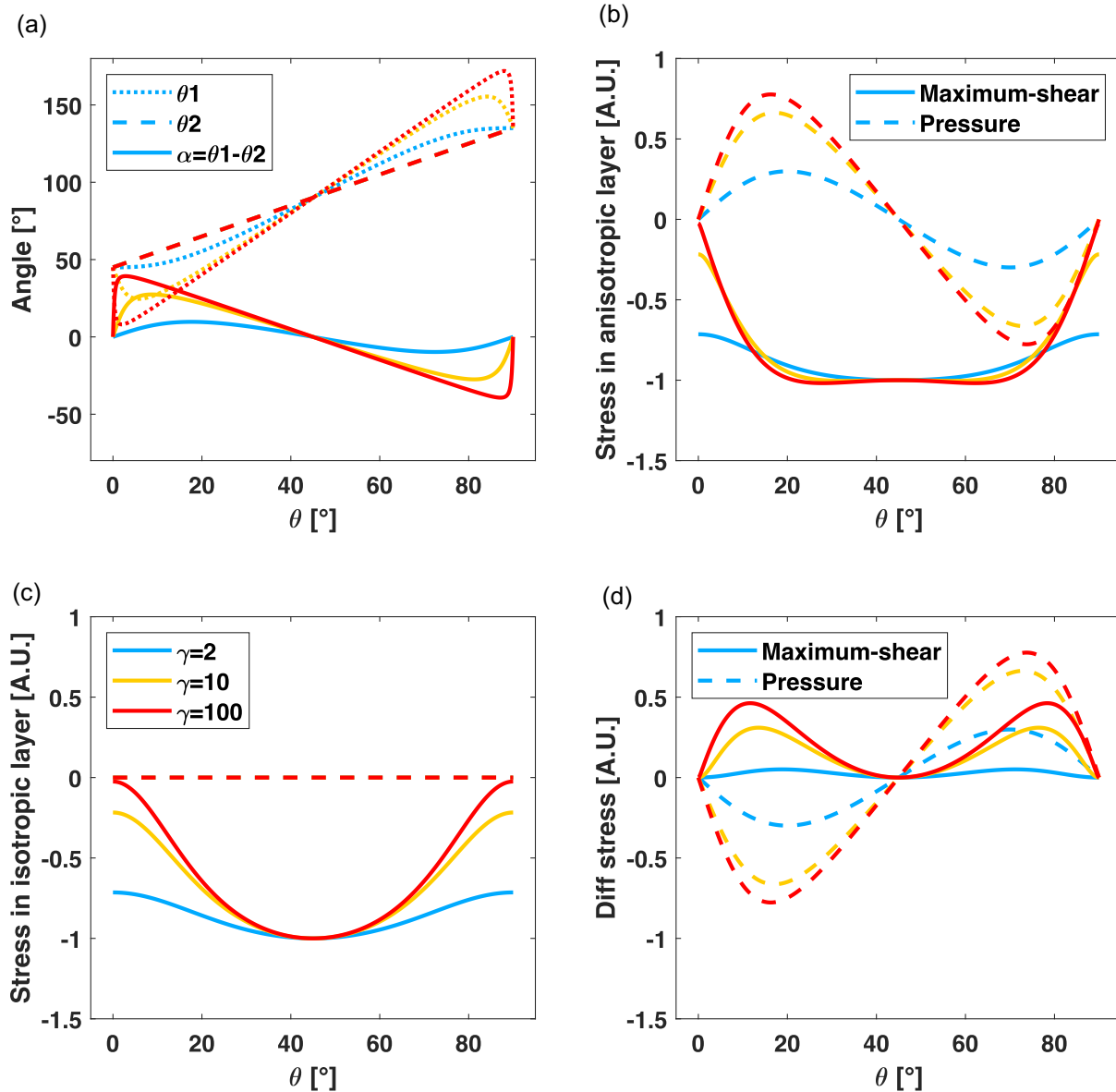


Figure 3. (a) Angular relations between principal stress σ_1 , principal strain rate $\dot{\epsilon}_1$ and the normal director \mathbf{n} of the weak anisotropic viscosity for three viscosity contrasts γ_s . Maximum shear stress and pressure as a function of θ in the anisotropic (b) and isotropic layer (c) for three γ values. (d) The difference between (b) and (c).

Figs 3(b) and (c) show the maximum shear stress σ_{xy}^{\max} and pressure p in the anisotropic layer and the isotropic layer, respectively, as a function of θ and γ . Fig. 3(d) shows the difference between Figs 3(b) and (c), and the difference shows similar trends as to the mismatch α that increases to a maximum and then decreases to zero when θ varies from 0° to 45° . For $\gamma = 2, 10$ and 100 , the difference of σ_{xy}^{\max} is $0.05, 0.31$ and 0.45 , which occur when $\theta = 18.8^\circ, 13.5^\circ$ and 11.6° , respectively.

The weak viscous anisotropy enhances strain rate in the anisotropic layer. The enhancement can be measured by ϕ , the strain-rate enhancement as defined in eq. (26). Fig. 5 shows the normalized strain-rate enhancement ϕ/γ , caused by various viscosity contrast γ_s as a function of θ . The maximum strain-rate enhancement occurs when $\theta = 0^\circ$ with a normalized value of unity, that is, the enhancement $\phi = \gamma$. The strain-rate enhancement decreases with increasing θ until there is no strain-rate enhancement with $\phi = 1$ when $\theta = 45^\circ$.

3 NUMERICAL SOLUTIONS FOR 2-D AND 3-D PROBLEMS

3.1 Overview of the finite-element method and formulations of various viscous anisotropy

For increased transparency, accessibility and expandability for more complicated 2-D and 3-D scenarios, including for regional settings, we develop a new finite-element code using the open-source computing platform *FEniCS* with a user-friendly Python interface (Logg & Wells 2010; Logg et al. 2012, <https://fenicsproject.org/>) to simulate incompressible Stokes flow with viscous anisotropy. The finite-element implementation follows the *FEniCS* Stokes tutorial (link provided in the Data and Software Statement). The material matrix for viscous anisotropy is fully expressed by fourth-order tensors through a set of Python functions, which currently support transversely isotropic and orthorhombic anisotropy,

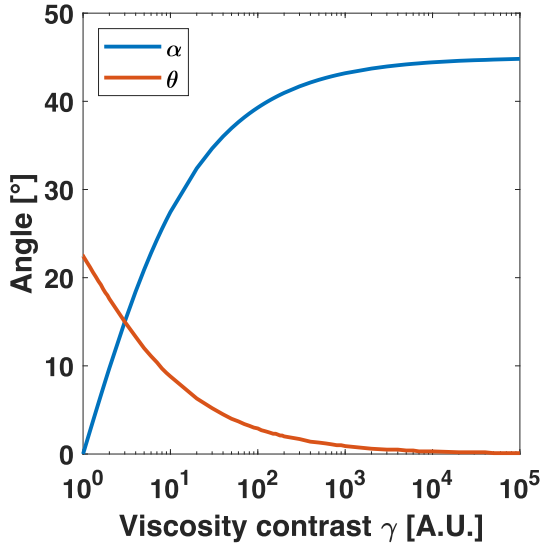


Figure 4. Maximum angular mismatch α between principal stress σ_1 and principal strain rate $\dot{\epsilon}_1$ as a function of viscosity contrast γ . For each γ , θ defines the normal vector of weak anisotropic direction at which the maximum α occurs.

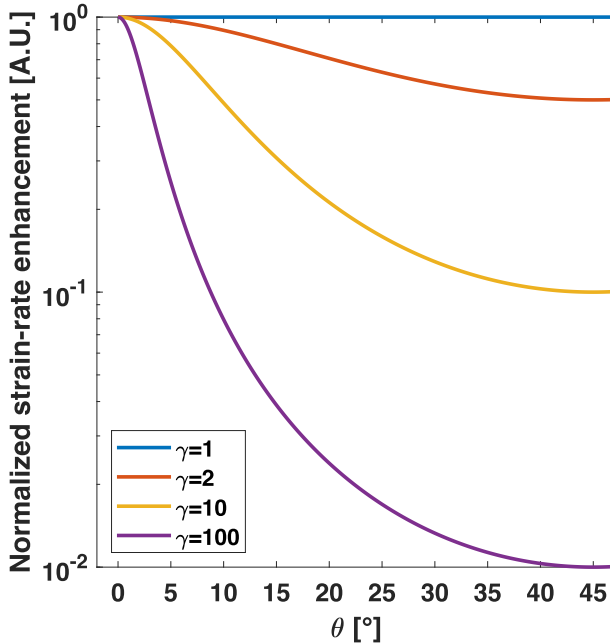


Figure 5. Normalized strain-rate enhancement ϕ/γ as a function of θ and for a range of viscosity contrasts γ . Strain-rate enhancement ϕ and γ are defined in eq. (26).

and can be readily expanded to anisotropy with more general symmetries.

For the choices of function spaces, we use second-order Continuous Galerkin (CG2) elements for velocity, and first-order Continuous Galerkin (CG1) elements for pressure in 2-D. For 3-D problems, we use third-order Continuous Galerkin (CG3) elements for velocity, and second-order Discontinuous Galerkin (DG2) elements for pressure. The choices of the function space pairs satisfy the Ladyzhenskaya–Babuška–Brezzi (or inf-sup) compatibility condition (see Brezzi & Fortin 1991, for more details). The theoretical considerations behind the choices are described in Logg *et al.* (2011,

chap. 20), and references therein. We use built-in mesh generator of *FEniCS* with triangles in 2-D and tetrahedrals in 3-D for simple model geometries, and the open-source mesh generator *Gmsh* (Geuzaine & Remacle 2009, <https://gmsh.info/>) for more complicated model geometries. *FEniCS* provides API to *Gmsh* for a seamless integration of the two tools.

We solve the system of linear equations assembled from the finite-element system with the open-source solution *PETSc* (<https://petsc.org/release/>), which is integrated with *FEniCS*. Direct solver *MUMPS* and preconditioned iterative *Krylov* solvers that come with *PETSc*s are used. In *FEniCS*, 2-D and 3-D, and serial and parallel versions of the code share similar syntax with minimal changes, which greatly reduces the cost of development when scaling to large problems is required. The finite-element code and associated post-processing tools are available publicly via the *GitHub* repository (link provided in the Data and Software Availability Statement).

Here, we present the weak form of the Stokes equations and mathematical formulations for various anisotropy that are implemented. From the strong form of the incompressible Stokes flow eqs (1)–(3), and the boundary condition eq. (9), the weak form of the Stokes equations are formulated in a mixed variational form with two variables, the velocity \mathbf{v} and pressure p , that are approximated simultaneously, after multiplying test functions \mathbf{u} and q , integrating over the domain, and integrating the gradient terms by parts,

$$a((\mathbf{v}, p), (\mathbf{u}, q)) = L((\mathbf{u}, q)), \quad (27a)$$

$$a((\mathbf{v}, p), (\mathbf{u}, q)) = \int (\nabla \mathbf{v} \cdot \nabla \mathbf{u} + \nabla \cdot \mathbf{u} p + \nabla \cdot \mathbf{v} q) dx, \quad (27b)$$

$$L((\mathbf{u}, q)) = \int \mathbf{f} \cdot \mathbf{u} dx + \int \mathbf{g} \cdot \mathbf{u} ds, \quad (27c)$$

where a and L are bilinear and linear terms of the variational formulation, \mathbf{g} is the flux on the Neumann boundary.

Following the Stokes tutorial, the sign of pressure is flipped from the strong form given above. The purpose is to have a symmetric but not positive-definite system of equations in the finite-element implementation, which can be solved iteratively after properly preconditioning of the system. We pre-condition the linear system of equations with the pre-conditioner defined as

$$b((\mathbf{v}, p), (\mathbf{u}, q)) = \int (\nabla \mathbf{v} \cdot \nabla \mathbf{u} + p q) dx. \quad (28)$$

Viscous anisotropy can be decomposed into components with different symmetries, for example, similarly to what was explored by Browaeys & Chevrot (2004) for elastic anisotropy in the Voigt approximation. Here, we derive and compare 3-D mathematical formulations of transversely isotropic anisotropy, which describe physical structures with a weak plane as shown in MM TI anisotropy, and orthorhombic anisotropy, which is a closer approximation to full crystal structure of olivine, here modelled under the incompressible fluid assumption.

We define local material coordinate system with axes 1, 2, 3, and finite-element coordinate system with axes x, y, z . To simplify the structure of the fourth-order viscosity tensor expressed as a 6×6 Voigt matrix form, axes to symmetry planes in viscosity are aligned with axes 1, 2 and 3. Different formulations for transversely isotropic viscous anisotropy are in use. With the deviatoric stress vector and strain-rate tensor defined as $\boldsymbol{\sigma} = (\sigma_{11}, \sigma_{22}, \sigma_{33}, \sigma_{23}, \sigma_{13}, \sigma_{12})$ and $\dot{\boldsymbol{\epsilon}} = (\dot{\epsilon}_{11}, \dot{\epsilon}_{22}, \dot{\epsilon}_{33}, 2\dot{\epsilon}_{23}, 2\dot{\epsilon}_{13}, 2\dot{\epsilon}_{12})$, following eq. (8), the Voigt form viscosity matrix \mathbf{V}^{MM} of MM TI

anisotropy is

$$\mathbf{V}^{\text{MM}} = \begin{bmatrix} 2\eta & 0 & 0 & & & \\ 0 & 2\eta & 0 & & & \\ 0 & 0 & 2\eta & & & \\ & & & \eta_S & 0 & 0 \\ & & & 0 & \eta & 0 \\ & & & 0 & 0 & \eta_S \end{bmatrix}, \quad (29)$$

where η is a reference shear viscosity and η_S is the weak anisotropic viscosity.

Han & Wahr (1997) derive a transversely isotropic viscous anisotropy from a different method, and the Voigt form viscosity matrix \mathbf{V}^{HW} is

$$\mathbf{V}^{\text{HW}} = \begin{bmatrix} \eta_1 + 2\nu_1 & 0 & \eta_1 & & & \\ 0 & \eta_2 + 2\nu_2 & 0 & & & \\ \eta_1 & 0 & \eta_1 + 2\nu_1 & & & \\ & & & \nu_2 & 0 & 0 \\ & & & 0 & \nu_1 & 0 \\ & & & 0 & 0 & \nu_2 \end{bmatrix}, \quad (30)$$

where ν_1 and ν_2 are isotropic shear and weak shear anisotropic viscosities, respectively. And η_1 (or η_2) corresponds to ‘normal’ anisotropic viscosity (see e.g. Christensen 1987). Not all four non-zero parameters are independent. Following the derivations in Han & Wahr (1997), $\boldsymbol{\sigma} = \mathbf{V}^{\text{HW}} \dot{\boldsymbol{\epsilon}}$ gives

$$\sigma_{11} = (\eta_1 + 2\nu_1) \dot{\epsilon}_{11} + \eta_1 \dot{\epsilon}_{33}, \quad (31a)$$

$$\sigma_{22} = (\eta_2 + 2\nu_2) \dot{\epsilon}_{22} \quad (31b)$$

$$\sigma_{33} = \eta_1 \dot{\epsilon}_{11} + (\eta_1 + 2\nu_1) \dot{\epsilon}_{33} \quad (31c)$$

The incompressible fluid assumption is,

$$\dot{\epsilon}_{11} + \dot{\epsilon}_{22} + \dot{\epsilon}_{33} = 0 \quad (32)$$

and zero of the trace of deviatoric stress tensor gives

$$\sigma_{11} + \sigma_{22} + \sigma_{33} = 0. \quad (33)$$

Substituting eqs (31) to eq. (33), we get

$$(2\eta_1 + 2\nu_1) \dot{\epsilon}_{11} + (\eta_2 + 2\nu_2) \dot{\epsilon}_{22} + (2\eta_1 + 2\nu_1) \dot{\epsilon}_{33} = 0. \quad (34)$$

To ensure eq. (32) is satisfied for any strain-rate tensor, eq. (34) gives

$$2\eta_1 + 2\nu_1 = \eta_2 + 2\nu_2. \quad (35)$$

The difference between \mathbf{V}^{MM} and \mathbf{V}^{HW} are the off-diagonal terms V_{13}^{HW} and V_{31}^{HW} . If $\eta_1 = 0$, \mathbf{V}^{HW} collapses to \mathbf{V}^{MM} , that is MM TI anisotropy is a simplified version of HW transversely isotropic without the correlation of deformation of normal strain rates inside the weak plane.

For orthorhombic anisotropy, we add on top of \mathbf{V}^{HW} an additional orthorhombic component inferred from analogy to the orthorhombic elastic tensor in Browaeys & Chevrot (2004), which we define as

$$\delta\mathbf{V}^{\text{ORTHOR}} = \begin{bmatrix} -a & b & 0 & & & \\ b & 0 & c & & & \\ 0 & c & a & & & \\ & & & -d & 0 & 0 \\ & & & 0 & 0 & 0 \\ & & & 0 & 0 & d \end{bmatrix}, \quad (36)$$

where a , b , c and d are non-zero parameters.

Then, the orthorhombic viscosity matrix $\mathbf{V}^{\text{ORTHOR}}$ is

$$\mathbf{V}^{\text{ORTHOR}} = \mathbf{V}^{\text{HW}} + \delta\mathbf{V}^{\text{ORTHOR}}, \quad (37a)$$

$$\mathbf{V}^{\text{ORTHOR}} = \begin{bmatrix} \eta_1 + 2\nu_1 - a & b & \eta_1 & & & \\ b & \eta_2 + 2\nu_2 & c & & & \\ \eta_1 & c & \eta_1 + 2\nu_1 + a & & & \\ & & & \nu_2 - d & 0 & 0 \\ & & & 0 & \nu_1 & 0 \\ & & & 0 & 0 & \nu_2 + d \end{bmatrix}. \quad (37b)$$

The four non-zero parameters are not all independent given the incompressible fluid assumption. Following the same method above, $\boldsymbol{\sigma} = \mathbf{V}^{\text{ORTHOR}} \dot{\boldsymbol{\epsilon}}$ gives

$$\sigma_{11} = (\eta_1 + 2\nu_1 - a) \dot{\epsilon}_{11} + b \dot{\epsilon}_{22} + \eta_1 \dot{\epsilon}_{33}, \quad (38a)$$

$$\sigma_{22} = b \dot{\epsilon}_{11} + (\eta_2 + 2\nu_2) \dot{\epsilon}_{22} + c \dot{\epsilon}_{33}, \quad (38b)$$

$$\sigma_{33} = \eta_1 \dot{\epsilon}_{11} + c \dot{\epsilon}_{22} + (\eta_1 + 2\nu_1 + a) \dot{\epsilon}_{33}. \quad (38c)$$

Substituting eqs (38) into eq. (33), we get

$$(2\eta_1 + 2\nu_1 - a + b) \dot{\epsilon}_{11} + (b + c + \eta_2 + 2\nu_2) \dot{\epsilon}_{22} + (2\eta_1 + 2\nu_1 + a + c) \dot{\epsilon}_{33} = 0. \quad (39)$$

To ensure eq. (32) is satisfied for any strain-rate tensor, and combining eq. (35), $a = b = -c$. Therefore, of the four non-zero parameters, only a and d are independent.

Rotations of fourth-order viscosity tensor are required to translate viscosity matrix from the material coordinate system to the finite-element one, and vice versa. In later 3-D scenarios with the anisotropic shear zone under simple shearing, we consider two elementary rotations of material coordinate system relative to the finite-element coordinate system, as shown in Fig. 9. Axes 1, 2 and 3 are originally aligned with axes x , y and z . For transversely isotropic anisotropy, axis 2 is the normal director to the weak viscosity plane. For the first elementary rotation, axis 2 is rotated counterclockwise away from axis y around axis z for an angle of θ . This rotation is like the rotation of \mathbf{n} in the 2-D analytical model. For the second elementary rotation, axes 1 and 3 are further rotated around axis 2 counterclockwise for an angle of β .

In the following sections, we first verify the finite-element implementation against the analytical solution by modelling the same problem presented in Section 2. We then increase the complexity slightly by introducing a Gaussian distribution of weak anisotropy across the thickness of the anisotropic layer. We next simulate a set of 2-D models inspired by a vertical fossil shear zone subjected to misoriented shortening to explore the strain-rate enhancement caused by the mechanical anisotropy. Then, 3-D shear zones with orthorhombic and two forms of transversely isotropic anisotropy subjected to simple shearing are simulated. Lastly, we present results from a 3-D model inspired by the Leech River Schist (LRS) above the Cascadia subduction zone (Bostock & Christensen 2012, and references therein) under convergent margin loading conditions.

3.2 Verification of the *FEniCS* code against the analytical solution

We simulate the 2-D model in Fig. 1 with our *FEniCS* code and verify the implementation against analytical solutions derived in Section 2. Fig. 6 shows matching *FEniCS* and analytical solutions for velocity, strain-rate enhancement, effective stress and pressure

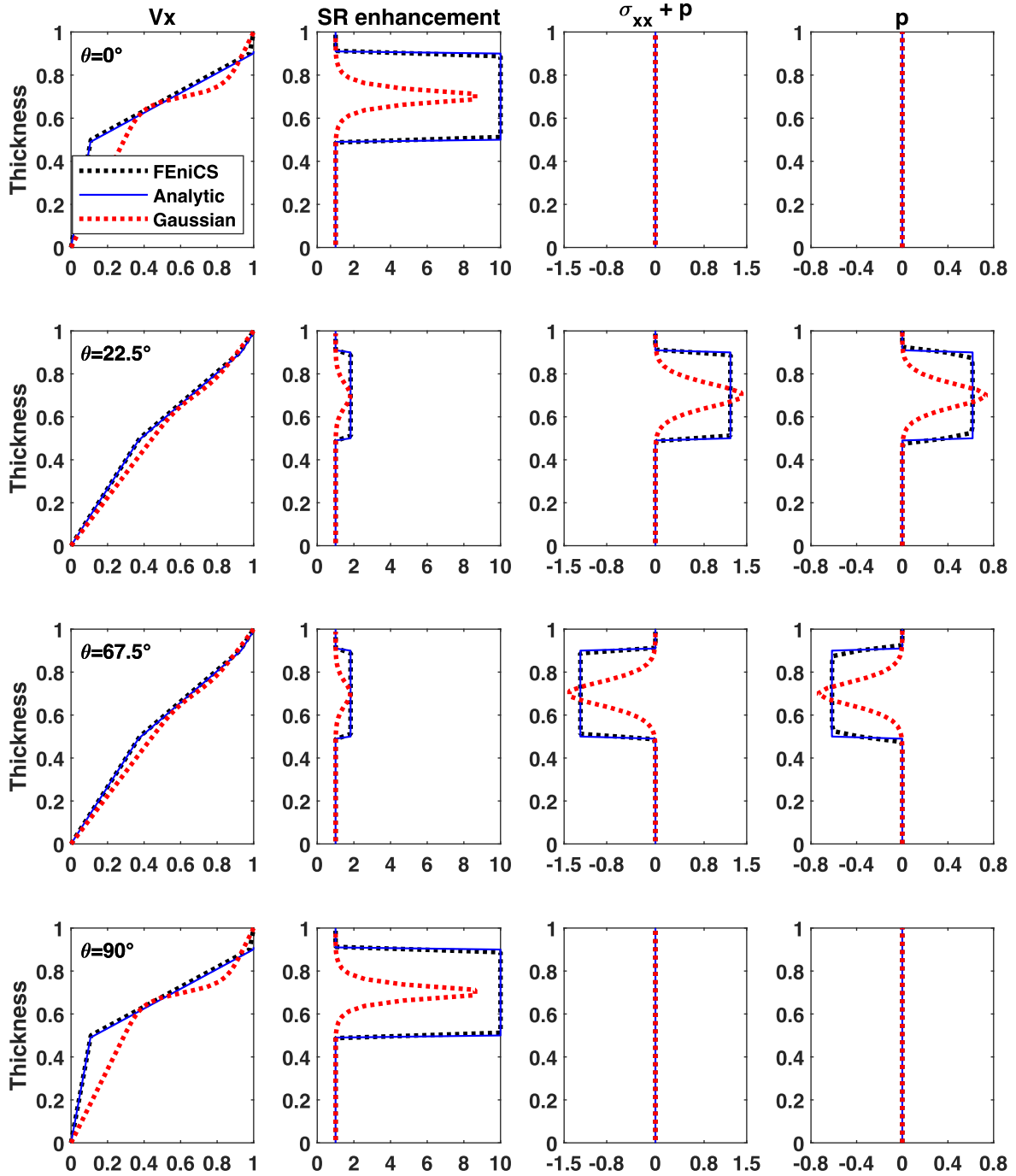


Figure 6. Verification of *FEniCS* finite-element solution against analytical solution for horizontal velocity, v_x , strain-rate enhancement, effective stress $\sigma_{xx} + p$ and pressure p , over thickness. Results with weak anisotropy following a Gaussian distribution in the anisotropic layer are in red lines. θ denotes the orientation of weak anisotropy director defined in Fig. 1.

over the whole thickness of the model, indicating that the code correctly implements this case of anisotropy.

These analytical solutions were also reproduced by our earlier numerical implementations of MM TI anisotropy in the *CitcomCU* (Moresi & Solomatov 1995; Zhong *et al.* 1998) and *CitcomS* (Zhong *et al.* 2000; Tan *et al.* 2006) convection code base (Becker & Kawakatsu 2011), as was used by Ghosh *et al.* (2013), for example.

Fig. 6 also shows results of a scenario with Gaussian distribution of weak anisotropy where $\eta_S = 1 - (1 - \frac{1}{\gamma}) \exp(-(\frac{y-y_c}{Th})^2)$,

perhaps closer to what might be expected in a natural shear zone. Here, $y_c = -0.7$ is the thickness at the centre of the anisotropic layer, $Th = 0.1$, and γ is 10. η_S is $\frac{1}{\gamma} = 0.1$ at y_c , and about unity, that is, the isotropic shear viscosity, when y approaches the edges of the anisotropic layer ($y = -0.5$ and -0.9). The η_S in the Gaussian scenario is mostly larger than the constant 0.1 in the analytical solution over the anisotropic layer. Therefore, amplitudes of heterogeneities of strain-rate enhancement, stress and pressure are less pronounced compared to the analytical solution and the peaks occur within a narrower thickness.

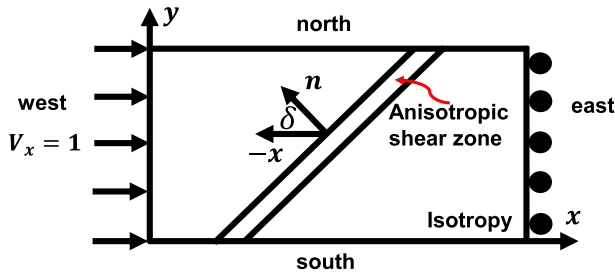


Figure 7. (a) Schematic diagram of 2-D shear zone subjected to misoriented shortening. The west side has a unit shortening of $v_x = 1$ and the east side is free slip. The north and south sides are either free or extruding at a fixed velocity. The shear zone is at an angle of δ to the unit shortening. \mathbf{n} , the normal director to the weak anisotropy, is always normal to the shear zone strike.

3.2 ‘Fossil mantle’ shear zone subjected to misoriented shortening

We now consider strain-rate enhancements from a set of models with anisotropic shear zones subjected to misoriented shortening, partially inspired by the work of Mameri *et al.* (2021) and our earlier exploration of potential signals of mechanical anisotropy in southern California (Schulte-Pelkum *et al.* 2021).

The anisotropic shear zone is characterized by MM TI anisotropy with the weak plane aligned with the strike of the shear zone. We simulate the deformation and stress/pressure from 2-D models of 2.5 by 1 along x - and y -directions, respectively, with viscosity contrast $\gamma = 10$. The shear zone width is 0.1 and it is striking at an angle of δ to the unit shortening ($v_x = 1$) along x on the west side (Fig. 7a). The east side is free slip.

For the north and south sides, two scenarios are considered. In the Free Sides scenario, both sides are free, which simulates the extreme condition that the interacting blocks outside of the north and south of the domain are extremely weak. In the Pure Shear scenario, the north and south sides extrude at absolute velocities of $|v_y| = 0.2$, simulating the other extreme condition that the interacting blocks are sufficiently strong compared to the simulated domain. Because we are solving incompressible Stokes flow, the extruding velocity of 0.2 is calculated by conserving the total volume. We vary δ from 5° to 65° in 5° step size. We also consider scenarios with the shear zone to be isotropic but with weaker viscosity $\frac{1}{\gamma} = 0.1$ than the surroundings.

The weak viscosity in the shear zone enhances strain-rates. The enhancement depends on the style of rheology and boundary conditions. Fig. 8 shows strain-rate enhancement caused by the weak shear zone for various δ s, the angle between the normal to the shear zone strike and the horizontal shortening. The strain-rate enhancement is calculated by the average of square root of J_2 invariant of the strain-rate tensor in the shear zone divided the average outside of the shear zone along a horizontal profile. For Free Sides scenarios, if the shear zone is MM TI anisotropy, the maximum strain-rate enhancement reaches 10, the same as the viscosity contrast $\gamma = 10$ given, when $\delta = 45^\circ$. If the shear zone is isotropic weak $\eta^{\text{iso}} = 0.1$, the maximum strain-rate enhancement is ~ 5.4 . Either by increasing or decreasing δ away from 45° , strain-rate enhancement decreases.

The maximum strain-rate enhancement with the isotropic weak shear zone is lower than for the MM TI anisotropy due to lower shear stress along the inclined shear zone. The driving force is normal stress τ_{xx} , which mainly affects flow $\dot{\epsilon}_{xx}$ through the corresponding

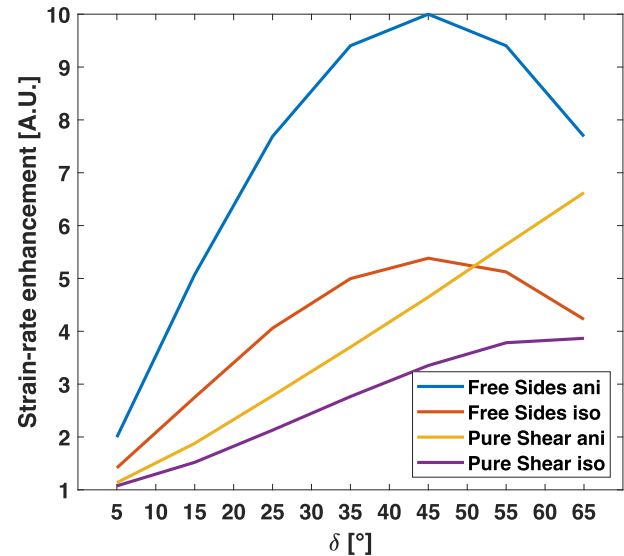


Figure 8. Strain-rate enhancement caused by 2-D weak viscous shear zone subjected to misoriented shortening.

normal viscosity. In the isotropic weak shear zone, not only the shear viscosity is lower than the isotropic surrounding, as in the MM TI anisotropic shear zone, but also the normal viscosities are lower than those in both the isotropic surrounding and MM shear zone. As a result, stresses and pressure are heterogeneous across the shear zone in the isotropic weak scenario, while they are homogenous for MM scenario. In particular, τ_{xx} is lower inside the isotropic shear zone, which leads to lower shear stress along the inclined shear zone.

The boundary conditions also matter. Mameri *et al.* (2021) discussed the effect of boundary conditions with free slip/lithospheric pressure conditions given their viscoelastic rheology. In our models, the north and south sides in Pure Shear scenarios are more restricted compared to Free Sides scenarios where material is free to flow along the shear zone and outwards the north and south sides. As shown in Fig. 8, for either anisotropic or isotropic weak shear zone, Pure Shear scenarios give less strain-rate enhancement compared to Free Sides scenarios. The maximum strain-rate enhancement occurs when $\delta = 65^\circ$ and it decreases with decreasing δ . Pure Shear isotropic weak shear zone produces less strain-rate enhancement compared to anisotropic scenarios.

3.3 3-D shear zone with transversely isotropic and orthorhombic anisotropy under simple shearing

We simulate 3-D shear zones with MM and HW transversely isotropic anisotropy and orthorhombic anisotropy under simple shearing. Fig. 9 shows the unit box that has the anisotropic zone enclosed by isotropic layers. The north side has a unit velocity along x . The top, bottom and south sides are free slip, and the east and west sides are periodic for both velocity and pressure. The volume of the model does not change, compatible to the incompressible fluid assumption.

Following the decomposition method in Browaeys & Chevrot (2004), we can compute the contributions to viscosity from isotropic, transversely isotropic and orthorhombic symmetries.

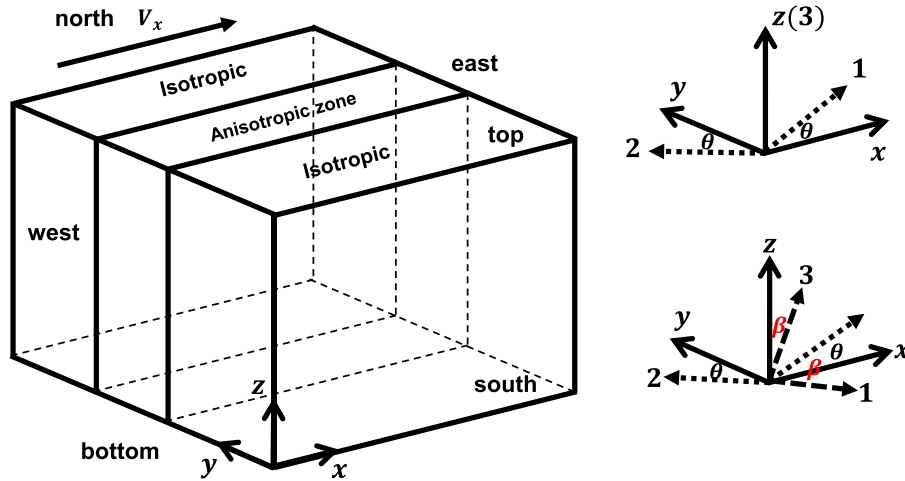


Figure 9. Diagram of 3-D anisotropic shear zone under simple shearing. Two elementary rotations from local material coordinate system 1, 2 and 3 that define the Voigt form of viscosity matrix, to finite-element coordinate system x, y, z are shown.

Tetragonal and other lower symmetries such triclinic and monoclinic in the viscosity are not included in this study. As a demonstration, we choose $\eta = 1, \eta_s = 0.1, \eta_1 = 0.3, a = 0.6$ and $d = 0$, which parameters give ~ 76 per cent isotropic and ~ 24 per cent transversely isotropic component weights for MM TI anisotropy, and ~ 70 per cent isotropic and ~ 21 per cent transversely isotropic and 9 per cent orthorhombic component weights for ORTHOR anisotropy, analogous to the composition of elasticity tensor of olivine.

We simulate models with θ from 0° to 90° at 10° step size, and β from 0° to 90° at 15° step size. Figs 10(a) and (b) show the mismatch of principal stress and strain-rate axes at the centre ($x = 0.5, y = 0.5$ and $z = 0.5$) of the anisotropic zone for ORTHOR and MM TI anisotropy, respectively. For $\theta = 0^\circ$ or 90° , the mismatch is zero for both ORTHO and MM TI anisotropy, consistent with results from 2-D models. For other θ s but same β , mismatch peaks at $\theta = 10^\circ$ or 80° and decreases when θ changes toward 45° . The mismatch for MM TI anisotropy does not depend on β , as expected from the fact that transversely isotropic anisotropy is isotropic inside the

weak plane. The mismatch angles are the same as the 1-D analytical solutions for same θ s in Fig. 3(a). In contrast, the mismatch for ORTHOR anisotropy depends on β and increases when β increases from 0° to 90° ($V_{33}^{\text{ORTHOR}} < V_{22}^{\text{ORTHOR}} < V_{11}^{\text{ORTHOR}}$) for most θ s except for $\theta = 40^\circ$ or 50° . For one θ , the spread of mismatch for different β s ranges from $\sim 5^\circ$ ($\theta = 10^\circ$ or 80°) to $\sim 2^\circ$. HW transversely isotropic anisotropy gives the same mismatch angle results to MM anisotropy.

In addition to the β -dependence of mismatch for ORTHOR anisotropy, it tilts the principal stress and strain-rate axes out of the horizontal x - y plane. Figs 11(a) and (b) show the dip angles of axes of (a) principal stress and (b) strain rate at the centre of the ORTHOR anisotropic zone for θ s and β s. The axes of principal stress do not dip much. Larger dips occur with $\theta > 40^\circ$. The peak dip is $\sim 2^\circ$ when $\theta = 80^\circ$ and $\beta = 30^\circ/45^\circ$ (Fig 12a). The dips of axes of principal strain-rates show higher values when $\theta < 60^\circ$ with peak value at $\sim 7^\circ$ when $\theta = 20^\circ$ and $\beta = 45^\circ$ (Fig 12b). For transversely isotropic anisotropy, the principal axes all stay inside the horizontal x - y plane.

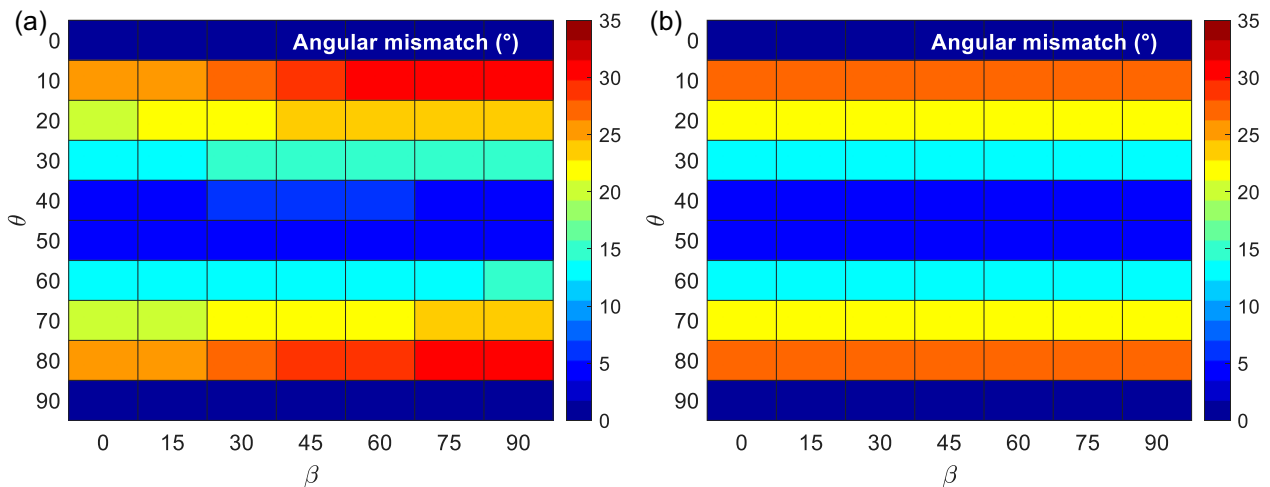


Figure 10. Angular mismatch of principal stress and strain-rate axes for (a) orthorhombic and (b) Muhlhaus and Moresi transversely isotropic (MM TI) anisotropy at the centre of the anisotropic zone in the 3-D model subjected to simple shearing.

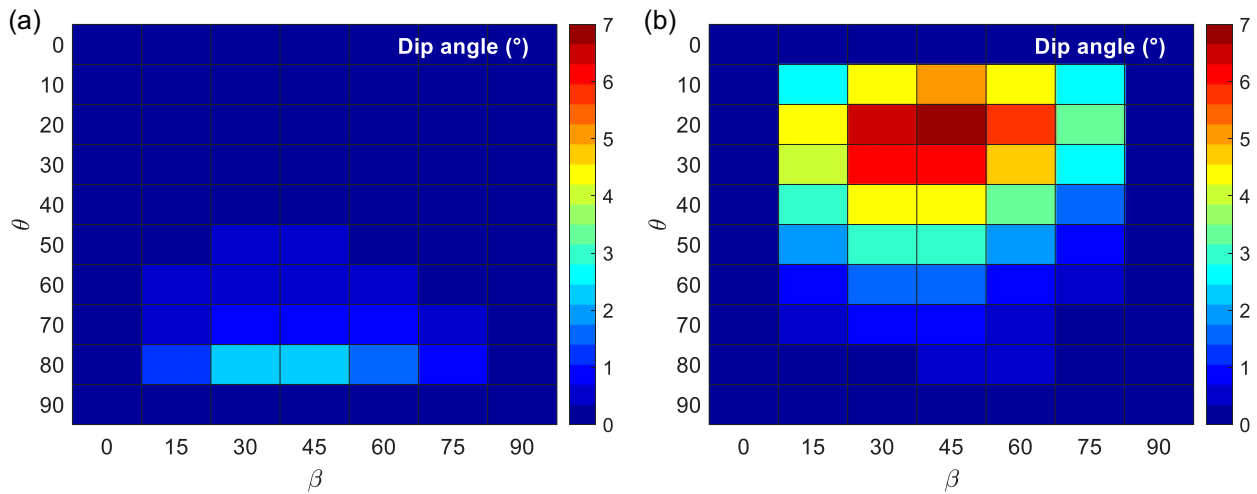


Figure 11. Dips of axes of (a) principal stress and (b) strain rate at the centre of the orthorhombic anisotropic zone for different θ s and β s.

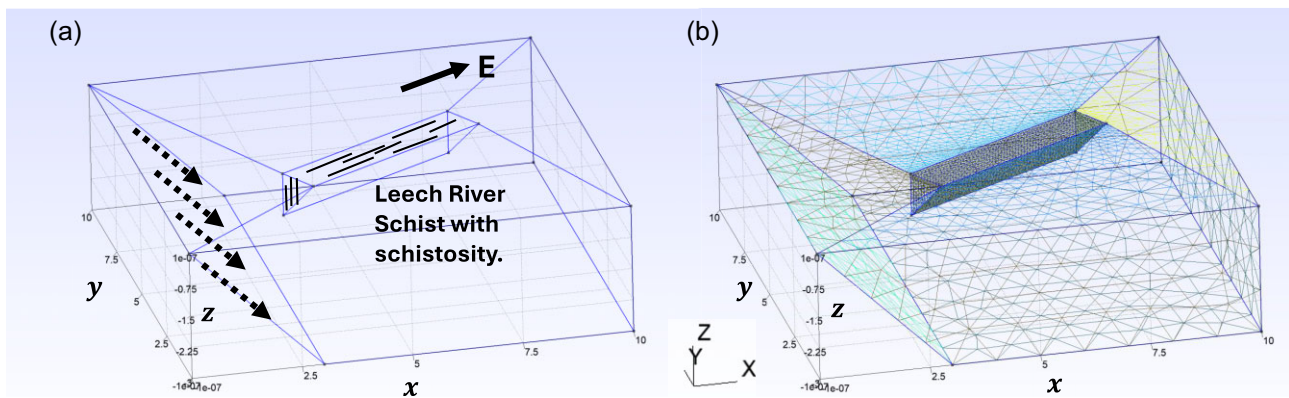


Figure 12. (a) Finite-element model of the LRS model. The schist is at the centre of the model with west–east trending and vertically dipping schistosity. East is indicated. Dashed lines show the subducting of the Juan de Fuca plate. Except for the free surface, other boundaries are free slip. (b) Tetrahedral finite-element mesh generated by the open-source mesh generator *Gmsh* with refined mesh inside the schist.

3.4 Leech River Schist above the Cascadia subduction zone

We expect that viscous anisotropy may arise from structural anisotropy like schist, rocks that has highly developed layered textures, which are generally exposed and associated with subduction zone environments (e.g. Chapman *et al.* 2010; Bostock & Christensen 2012; Chapman 2016; Xia & Platt 2017). It appears the schist may overlap on top of the subducting oceanic plate as reconstructed geologically in the southern California case (Xia & Platt 2017), though the schists were transferred to shallow depth in subsequent geologic episodes. If viscous anisotropy may cause non-coaxial stress/strain-rate axes and significant stress heterogeneity and enhance strain rates as we demonstrate in previous theoretical setups, the migration of schist and its close relation to subduction zones may play an important role in the tectonic deformation of the lithosphere. Here, we focus our attention to the non-coaxially of stress strain-rate axes from a regional wedge-shaped schist structure subjected to subducting loading.

In Cascadia between southern Puget Sound and central Vancouver Island, the LRS, which is bounded by two north dipping thrusts forming a wedge (Bostock & Christensen 2012, and references therein). The LRS rides on top of the subducting Juan de Fuca plate relative to North America. The schistosity, which is the parallel

alignment of platy mineral constituents that reflects a considerable intensity of metamorphism, is generally west–east and vertically dipping and the relative plate motion direction is N56° E (Bostock & Christensen 2012). Fig. 12 shows a finite-element model and boundary conditions inspired by the LRS. The model domain is dimensionless and 10 by 10 by 3 along x , y and z , respectively. The grid size inside the schist wedge is 0.1, which gradually increases to 1 near the model boundaries. The schist wedge is 2 by 1 on the free surface and vanishes at depth of -1 . The schist is assumed to be with MM TI anisotropy and the weak viscosity is aligned with the general strike of the schist, which is $\sim 60^\circ$ relative to the y -axis. The viscosity contrast is 10.

Fig. 13 presents the principal stress and strain-rate axes on three orthogonal cross-sections, x – y plane at $z = -0.5$, y – z plane at $x = 5$, and x – z plane at $y = 5$, that cut through the schist, respectively. The subducting loading and the wedge shape of the anisotropic regime are different from previous models and produce different stress and strain-rate axes patterns.

In map view (Fig. 13a), the whole schist shows non-coaxial stress and strain-rate axes with mismatch angles about $27^\circ - 30^\circ$. Strain-rate axes inside the anisotropic zone are largely aligned with those in the isotropic regime. The stress axes, on the other hand, are rotated away from those in the isotropic regime. The side view

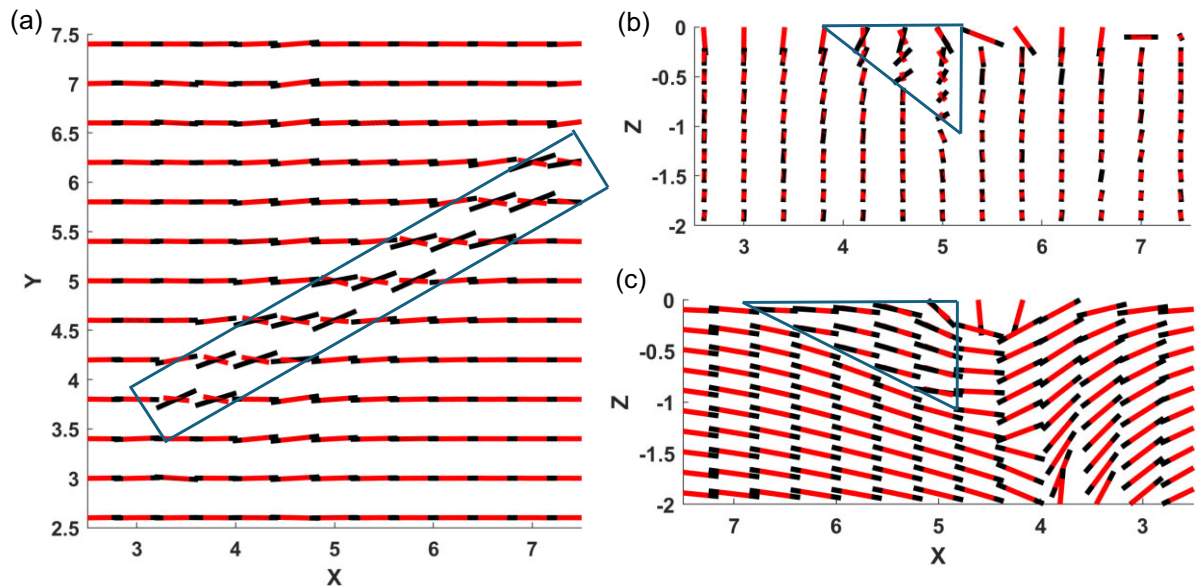


Figure 13. Principal stress (black, longer bar) and principal strain-rate (red, shorter bar) axes of a horizontal cross-section (a) at $z = -0.5$, of two vertical cross-sections (b) at $x = 5$ and (c) at $y = 5$ that cut through the LRS.

on the yz plane (Fig. 13b) also shows significant stress and strain-rate non-coaxiality with mismatch angles increase with depth. The mismatch could reach a notable 90° near the sharp wedge bottom. The other side view on xz plane (Fig. 13c) shows very limited angular mismatch of just a few degrees, when the subduction is near parallel to the weak direction of the anisotropy. In addition, the stress and strain-rate axes dip out of the horizontal plane. The implication is that loading style and the shape of anisotropic structure could be important in producing mismatch between principal stress and strain-rate axes, and dipping principal axes.

The results assume that the schist can be approximated with transversely isotropic viscous anisotropy and the deformation and stress features reflect the current loading condition. The schist may, of course, carry stress and strain signatures inherited from previous tectonic episodes and is subjected to temporal change depending on the viscosity of the structure and the time length-scale of interest. Further exploration of observations of stress and strain-rate orientations associated with the structure and a suite of models that have various viscosity contrasts would be helpful to differentiate signatures from present and inherited.

4 AN APPROACH TO CONSTRAIN VISCOUS ANISOTROPY

The difference of stress and pressure between the isotropic and anisotropic layers could influence mechanical processes in such a system like a fault zone (e.g. Hardebeck & Michael 2004; Hirano & Yamashita 2011). Non-coaxiality between principal stress and strain-rate axes from viscous anisotropy, such as due to SPOs and CPOs, could be assessed quantitatively, and they can infer stress and pressure heterogeneity. This motivates reassessment of independent measures for inferring stress or stressing rates (e.g. Michael 1984) and strain rates derived from geodetic constraints (e.g. Smith-Konter & Sandwell 2009). Close to faults in southern California, the two fields match in their alignment on broad scales, but there are also significant local deviations (Becker *et al.* 2005; Yang & Hauksson

2013; Schulte-Pelkum *et al.* 2021; Johnson 2024) which are expected to be of relevance for long-term tectonics as well as setting local stress conditions for earthquake rupture.

Schulte-Pelkum *et al.* (2021) discussed a wider range of deformation indicators for southern California from the surface to the asthenosphere mantle. They found general consistency with N-S compression and E-W extension near the surface and in the asthenospheric mantle, but all lithospheric anisotropy indicators deviate from such patterns. One interpretation was deformation memory from the Farallon subduction and subsequent extension.

Notably, a comparison of focal mechanism-based principal stress axes (Yang & Hauksson 2013) with GNSS-derived principal strain rates (Sandwell *et al.* 2016) shows an angular mismatch with a peaked distribution centred on an azimuth (CW from N) of -6° with a standard deviation of 19° (Schulte-Pelkum *et al.* 2021). Based on our results (Fig. 3a), the observations may indicate mild mechanical anisotropy of viscosity contrast of 2–10 in the region for nearly all the θ if we assume the weak anisotropy were parallel to the simple shearing loading. The higher viscosity contrast of 100 is also possible if $20^\circ < \theta < 70^\circ$. It could be also possible that the anisotropic structure is subjected to misoriented shortening or additional factors should be considered such as more complex loading conditions, special shapes of structures, inheritance from previous geodynamical processes, and combinations of any few. For misoriented orthorhombic anisotropy or the case of LRS where the loading is oblique to anisotropic regime with special shape, dips of principal axes could be used to infer mechanical anisotropy if they were measurable. Alternative sources that can help narrow down candidate scenarios are helpful.

The non-coaxiality of principal stress and strain-rate is more visible if the loading direction is misoriented from the weak anisotropic direction (cf. Ghosh *et al.* 2013). The case of LRS and the structure in southern California illustrate that the combining condition of misoriented loading and weak anisotropy (such as schistosity) may be common in nature. In addition to non-coaxial principal axes, heterogeneity of stress and pressure, and enhanced strain rate may

occur as well. For example, using teleseismic receiver functions, Audet (2015) finds that the plane of fast velocity strikes parallel to the SAF, while dipping mildly throughout the crust near Parkfield. He interprets the mid-crustal anisotropy as fossilized fabric within fluid-rich foliated mica schists. Our results suggest that heterogeneity of stress and pressure might indeed be induced by the mechanical anisotropy of the schist, which could influence the stress distribution in the region and nearby earthquakes.

5 CONCLUSION

We present a 1-D analytical solution to a viscously anisotropic layer subjected to simple shearing which predicts significant stress heterogeneity and non-coaxial stress and strain rates. Observations of the non-coaxiality and dips of principal axes could give us constraints on mechanical anisotropy in nature. Such analysis may be possible, for example, by comparing stress inversions from focal mechanisms, surface strain rates from geodetic measurements and integrated strain from seismic anisotropy (Schulte-Pelkum *et al.* 2021, and references therein).

To accelerate such studies, we develop an open-source finite-element code using *FEniCS*, verify the 2-D version of the code against the analytical solution, and explore several 2-D and 3-D illustrative cases with various loading styles, transversely isotropic and orthorhombic anisotropy, and the wedged shape LRS above the Cascadia subduction zone. We hope that this exploration of mechanical anisotropy for tectonic problems and our new implementation will help advance model and verification of mechanically anisotropic lithospheric models, and their implications, from long-term plate boundary evolution to fault loading and rupture propagation.

DATA AND SOFTWARE AVAILABILITY STATEMENT

The *FEniCS* codes, the *MATLAB* code for the analytical solution, and *MATLAB* post-processing scripts for the figures, simulation results, and documentation are hosted in the *GitHub* repository https://github.com/dunyuliu/Toolset_for_Mechanical_Anisotropy. *FEniCS* is available via <https://fenicsproject.org/>. We use the latest stable release of legacy *FEniCS* version 2019.1.0. The link to Stokes tutorial is <https://fenicsproject.org/olddocs/dolfin/1.3.0/python/demo/documented/stokes-iterative/python/documentation.html> *MATLAB* is available via <https://www.mathworks.com/>. Academic License is used in this work. *Gmsh* is available via <https://gmsh.info/>. Fabio Crameris's colour maps are used (Crameris 2018a, 2018b).

ACKNOWLEDGMENTS

DL, SP and TWB were partially funded by National Science Foundation EAR-2121666 and 1927216, and preliminary work was supported by the Southern California Earthquake Center contribution no. 11877. Southern California Earthquake Center is funded by National Science Foundation Cooperative Agreement EAR-1600087 and United States Geological Survey Cooperative Agreement G17AC00047. LM was supported by the Australian Research Council Discovery Scheme, DP150102887. We thank editors Juan Carlos Afonso and Gael Choblet, two reviewers Dr Angeles Kiraly and Dr Andréa Tommasi for comments and suggestions on an earlier version of this manuscript. We thank editor Henri Samuel and

reviewers Dr Andréa Tommasi and Dr Manuele Faccenda for comments on the revised manuscript.

REFERENCES

- Audet, P., 2015. Layered crustal anisotropy around the San Andreas Fault near Parkfield, California, *J. geophys. Res.—Solid Earth*, **120**, 3527–3543.
- Babuska, V. & Cara, M., 1991. *Seismic Anisotropy in the Earth*, Springer Science & Business Media.
- Becker, T.W. & Kawakatsu, H., 2011. On the role of anisotropic viscosity for plate-scale flow, *Geophys. Res. Lett.*, **38**, doi:10.1029/2011GL048584.
- Becker, T.W. & Lebedev, S., 2021. *Dynamics of the Upper Mantle in Light of Seismic Anisotropy*, First edn. John Wiley & Sons, Inc.
- Becker, T.W., Chevrot, S., Schulte-Pelkum, V. & Blackman, D.K., 2006. Statistical properties of seismic anisotropy predicted by upper mantle geodynamic models, *J. geophys. Res.—Solid Earth*, **111**, B08309, doi:10.1029/2005JB004095.
- Becker, T.W., Hardebeck, J.L. & Anderson, G., 2005. Constraints on fault slip rates of the southern California plate boundary from GPS velocity and stress inversions, *Geophys. J. Int.*, **160**, 634–650.
- Blackman, D.K., Boyce, D.E., Castelnau, O., Dawson, P.R. & Laske, G., 2017. Effects of crystal preferred orientation on upper-mantle flow near plate boundaries: rheologic feedbacks and seismic anisotropy, *Geophys. J. Int.*, **210**(3), 1481–1493.
- Bostock, M.G. & Christensen, N.I., 2012. Split from slip and schist: crustal anisotropy beneath northern Cascadia from non-volcanic tremor, *J. geophys. Res.—Solid Earth*, **117**, doi:10.1029/2011JB009095.
- Brezzi, F. & Fortin, M., 1991. *Mixed and Hybrid Finite Element Methods*. Springer Series in Computational Mathematics, Vol. 15, doi:10.1007/978-1-4612-3172-1.
- Browaays, J.T. & Chevrot, S., 2004. Decomposition of the elastic tensor and geophysical applications, *Geophys. J. Int.*, **159**, 667–678.
- Chapman, A.D., 2016. The Pelona–Orocopia–Rand and related schists of southern California: a review of the best-known archive of shallow subduction on the planet, *Int. Geol. Rev.*, **59**, 664–701.
- Chapman, A.D., Kidder, S., Saleeby, J.B. & Ducea, M.N., 2010. Role of extrusion of the Rand and Sierra de Salinas schists in late cretaceous extension and rotation of the southern Sierra Nevada and vicinity, *Tectonics*, **29**, doi:10.1029/2009TC002597.
- Chastel, Y.B., Dawson, P.R., Wenk, H.-R. & Bennett, K., 1993. Anisotropic convection with implications for the upper mantle, *J. geophys. Res.*, **98**(B10), 17757–17771.
- Christensen, U.R., 1985. Heat transport by variable viscosity convection II: pressure influence, non-Newtonian rheology and decaying heat sources, *Phys. Earth Planet. Int.*, **37**, 183–205.
- Christensen, U.R., 1987. Some geodynamical effects of anisotropic viscosity, *Geophys. J. R. astr. Soc.*, **91**, 711–736.
- Crameris, F., 2018a. Geodynamic diagnostics, scientific visualisation and StagLab 3.0, *Geosci. Model. Dev.*, **11**, 2541–2562.
- Crameris, F., 2018b. Scientific colour maps. doi:10.5281/zenodo.1243862.
- Geuzaine, C. & Remacle, J.F., 2009. *Gmsh: a 3-D finite element mesh generator with built-in pre- and post-processing facilities*, *Int. J. Numer. Method Eng.*, **79**, 1309–1331.
- Ghosh, A., Becker, T.W. & Humphreys, E.D., 2013. Dynamics of the North American continent, *Geophys. J. Int.*, **194**, 651–669.
- Han, D. & Wahr, J., 1997. An analysis of anisotropic mantle viscosity, and its possible effects on post-glacial rebound, *Phys. Earth planet. Inter.*, **102**, 33–50.
- Hansen, L.N., Warren, J.M., Zimmerman, M.E. & Kohlstedt, D.L., 2016. Viscous anisotropy of textured olivine aggregates, part 1: measurement of the magnitude and evolution of anisotropy, *Earth planet. Sci. Lett.*, **445**, 92–103.
- Hansen, L.N., Zimmerman, M.E. & Kohlstedt, D.L., 2012. Laboratory measurements of the viscous anisotropy of olivine aggregates, *Nature*, **492**, 415–418.

- Hardebeck, J.L. & Michael, A.J., 2004. Stress orientations at intermediate angles to the San Andreas Fault, California, *J. geophys. Res.—Solid Earth*, **109**. doi:10.1029/2004JB003239.
- Hirano, S. & Yamashita, T., 2011. Analysis of the static stress field around faults lying along and intersecting a bimaterial interface, *Geophys. J. Int.*, **187**, 1460–1478.
- Honda, S., 1986. Strong anisotropic flow in a finely layered asthenosphere. *Geophys. Res. Lett.*, **13**, 1454–1457.
- Johnson, K.M., 2024. Disagreements in geodetically inferred strain rates in the western US with stress orientations and geologic moment rates, *J. geophys. Res.—Solid Earth*, **129**(4), e2023JB027472, doi:10.1029/2023JB027472.
- Kaven, J.O., Maerten, F. & Pollard, D.D., 2011. Mechanical analysis of fault slip data: implications for paleostress analysis, *J. Struct. Geol.*, **33**, 78–91.
- Király, Á., Conrad, C.P. & Hansen, L.N., 2020. Evolving viscous anisotropy in the upper mantle and its geodynamic implications, *Geochem. Geophys. Geosyst.*, **21**, e2020GC009159, doi:10.1002/essoar.10503040.1.
- Lev, E. & Hager, B.H., 2008. Rayleigh-Taylor instabilities with anisotropic lithospheric viscosity, *Geophys. J. Int.*, **173**, 806–814.
- Lev, E. & Hager, B.H., 2011. Anisotropic viscosity changes subduction zone thermal structure, *Geochem. Geophys. Geosyst.*, **12**, doi:10.1029/2010GC003382.
- Logg, A. & Wells, G.N., 2010. DOLFIN: automated Finite Element computing, *ACM Trans. Math. Softw.*, **37**, 20, doi:10.1145/1731022.1731030.
- Logg, A., Mardal, K.-A. & Wells, G.N., 2011. *Automated Solution of Differential Equations by the Finite Element Method*, the FEniCS book, pp 381–394.
- Logg, A., Wells, G.N. & Hake, J., 2012. Chapter 10 DOLFIN: a C++/Python finite element library, in *Automated Solution of Differential Equations by the Finite Element Method*, pp. 173–225, eds. Logg, A., Mardal, K.-A. & Wells, G.N., Springer Berlin Heidelberg, Berlin, Heidelberg.
- Mameri, L., Tommasi, A., Signorelli, J. & Hassani, R., 2021. Olivine-induced viscous anisotropy in fossil strike-slip mantle shear zones and associated strain localization in the crust, *Geophys. J. Int.*, **224**, 608–625.
- Michael, A.J., 1984. Determination of stress from slip data—faults and folds, *J. geophys. Res.*, **89**, 1517–1526.
- Montési, L.G.J., 2013. Fabric development as the key for forming ductile shear zones and enabling plate tectonics, *J. Struct. Geol.*, **50**, 254–266.
- Moresi, L. & Mühlhaus, H.B., 2006. Anisotropic viscous models of large-deformation Mohr–Coulomb failure, *Philos. Mag.*, **86**, 3287–3305.
- Moresi, L., Dufour, F. & Mühlhaus, H.B., 2003. A lagrangian integration point finite element method for large deformation modeling of viscoelastic geomaterials, *J. Comput. Phys.*, **184**, 476–497.
- Moresi, L.N. & Solomatov, V.S., 1995. Numerical investigation of 2d convection with extremely large viscosity variations, *Phys. Fluids*, **7**, 2154–2162.
- Mühlhaus, H.B., Moresi, L. & Cada, M., 2004. Emergent anisotropy and flow alignment in viscous rock, *Pure appl. Geophys.*, **161**, 2451–2463.
- Mühlhaus, H.B., Moresi, L., Hobbs, B. & Dufour, F., 2002. Large amplitude folding in finely layered viscoelastic rock structures, *Pure appl. Geophys.*, **159**, 2311–2333.
- Perry-Houts, J. & Karlstrom, L., 2019. Anisotropic viscosity and time-evolving lithospheric instabilities due to aligned igneous intrusions, *Geophys. J. Int.*, **216**, 794–802.
- Rawling, G.C., Baud, P. & Wong, T., 2002. Dilatancy, brittle strength, and anisotropy of foliated rocks: experimental deformation and micromechanical modeling, *J. geophys. Res.—Solid Earth*, **107**, doi:10.1029/2001JB000472.
- Sandwell, D.T., Zeng, Y., Shen, Z.-K., Crowell, B., Murray, J., McCaffrey, R. & Xu, X., 2016. *The SCEC Community Geodetic Model VI: Horizontal Velocity Grid*. Tech. Rep. Scripps Institution of Oceanography, UCSD.
- Schmeling, H., 1985. Numerical models on the influence of partial melt on elastic, anelastic and electric properties of rocks. Part I: elasticity and anelasticity, *Phys. Earth planet. Inter.*, **41**(1), 34–57.
- Schulte-Pelkum, V., Becker, T.W., Behr, W.M. & Miller, M.S., 2021. Tectonic inheritance during plate boundary evolution in Southern California constrained from seismic anisotropy, *Geochem. Geophys. Geosyst.*, **22**, e2021GC010099, doi:10.1029/2021GC010099.
- Simons, F.J. & van der Hilst, R.D., 2003. Seismic and mechanical anisotropy and the past and present deformation of the Australian lithosphere, *Earth planet. Sci. Lett.*, **211**, 271–286.
- Smith-Konter, B. & Sandwell, D., 2009. Stress evolution of the San Andreas fault system: recurrence interval versus locking depth, *Geophys. Res. Lett.*, **36**, 10.1029/2009GL037235.
- Takei, Y. & Katz, R.F., 2013. Consequences of viscous anisotropy in a deforming, two-phase aggregate. Part 1. Governing equations and linearized analysis, *J. Fluid Mech.*, **734**, 424–455.
- Tan, E., Choi, E., Thoutireddy, P., Gurnis, M. & Aivazis, M., 2006. GeoFramework: coupling multiple models of mantle convection within a computational framework, *Geochem. Geophys. Geosyst.*, **7**, doi:10.1029/2005GC001155.
- Tommasi, A., Knoll, M., Vauchez, A., Signorelli, J., Thoraval, C. & Loge, R., 2009. Structural reactivation in plate tectonics controlled by olivine crystal anisotropy, *Nat. Geosci.*, **2**, 422–426.
- Vauchez, A., Tommasi, A. & Barruol, G., 1998. Rheological heterogeneity, mechanical anisotropy and deformation of the continental lithosphere, *Tectonophysics*, **296**, 61–86.
- Xia, H. & Platt, J.P., 2017. Structural and rheological evolution of the Laramide subduction channel in southern California, *Solid Earth*, **8**, 379–403.
- Yang, W.Z. & Hauksson, E., 2013. The tectonic crustal stress field and style of faulting along the Pacific North America Plate boundary in Southern California, *Geophys. J. Int.*, **194**, 100–117.
- Zhong, S.J., Gurnis, M. & Moresi, L., 1998. Role of faults, nonlinear rheology, and viscosity structure in generating plates from instantaneous mantle flow models, *J. geophys. Res.—Solid Earth*, **103**, 15255–15268.
- Zhong, S.J., Zuber, M.T., Moresi, L. & Gurnis, M., 2000. Role of temperature-dependent viscosity and surface plates in spherical shell models of mantle convection, *J. geophys. Res.—Solid Earth*, **105**, 11063–11082.